Astronomy & Astrophysics

High contrast at short separation with VLTI/GRAVITY: Bringing *Gaia* companions to light[*]

N. Pourré[1], T. O. Winterhalder[2], J.-B. Le Bouquin[1], S. Lacour[3,2], A. Bidot[1], M. Nowak[4], A.-L. Maire[1],
D. Mouillet[1], C. Babusiaux[1], J. Woillez[2], R. Abuter[2], A. Amorim[5,6], R. Asensio-Torres[7], W. O. Balmer[8,9],
M. Benisty[1], J.-P. Berger[1], H. Beust[1], S. Blunt[10], A. Boccaletti[3], M. Bonnefoy[1], H. Bonnet[2], M. S. Bordoni[11],
G. Bourdarot[11], W. Brandner[7], F. Cantalloube[12], P. Caselli[11], B. Charnay[3], G. Chauvin[13], A. Chavez[10],
E. Choquet[12], V. Christiaens[14], Y. Clénet[3], V. Coudé du Foresto[3], A. Cridland[15], R. Davies[11], D. Defrère[17],
R. Dembet[3], J. Dexter[16], A. Drescher[11], G. Duvert[1], A. Eckart[18,19], F. Eisenhauer[11], N. M. Förster Schreiber[11],
P. Garcia[6,20], R. Garcia Lopez[21,7], E. Gendron[3], R. Genzel[11,23], S. Gillessen[11], J. H. Girard[9], F. Gonte[2],
S. Grant[11], X. Haubois[24], G. Heißel[25,3], Th. Henning[7], S. Hinkley[26], S. Hippler[7], S. F. Hönig[22], M. Houllé[13],
Z. Hubert[1], L. Jocou[1], J. Kammerer[2], M. Kenworthy[15], M. Keppler[7], P. Kervella[3], L. Kreidberg[7],
N. T. Kurtovic[11], A.-M. Lagrange[1,3], V. Lapeyrère[3], D. Lutz[11], F. Mang[11], G.-D. Marleau[27,28,29,7], A. Mérand[2],
F. Millour[13], P. Mollière[7], J. D. Monnier[30], C. Mordasini[29], E. Nasedkin[7], S. Oberti[2], T. Ott[11], G. P. P. L. Otten[31],
C. Paladini[24], T. Paumard[3], K. Perraut[1], G. Perrin[3], O. Pfuhl[2], L. Pueyo[9], D. C. Ribeiro[11], E. Rickman[32],
Z. Rustamkulov[33], J. Shangguan[11], T. Shimizu[11], D. Sing[8,33], F. Soulez[40], J. Stadler[34,35], T. Stolker[15], O. Straub[35],
C. Straubmeier[18], E. Sturm[11], C. Sykes[22], L. J. Tacconi[11], E. F. van Dishoeck[15,11], A. Vigan[12], F. Vincent[3],
S. D. von Fellenberg[19], J. J. Wang[10], F. Widmann[11], and S. Yazici[11]
(GRAVITY Collaboration),
J. A. Abad[2], E. Aller Carpentier[2], J. Alonso[24], L. Andolfato[2], P. Barriga[2], J.-L. Beuzit[12], P. Bourget[24], R. Brast[2],
L. Caniguante[24], E. Cottalorda[13], P. Darré[2], B. Delabre[2], A. Delboulbé[1], F. Delplancke-Ströbele[2], R. Donaldson[2],
R. Dorn[2], C. Dupuy[2], S. Egner[2], G. Fischer[2], C. Frank[2], E. Fuenteseca[24], P. Gitton[24], T. Guerlet[2], S. Guieu[1],
P. Gutierrez[2], P. Haguenauer[2], A. Haimerl[2], C. T. Heritier[36,12], S. Huber[2], N. Hubin[2], P. Jolley[2], J.-P. Kirchbauer[2],
J. Kolb[2], J. Kosmalski[2], P. Krempl[37], M. Le Louarn[2], P. Lilley[2], B. Lopez[13], Y. Magnard[1], S. Mclay[2], A. Meilland[13],
A. Meister[24], T. Moulin[1], L. Pasquini[2], J. Paufique[2], I. Percheron[2], L. Pettazzi[2], D. Phan[2], W. Pirani[2], J. Quentin[2],
A. Rakich[2], R. Ridings[2], J. Reyes[2], S. Rochat[1], C. Schmid[2], N. Schuhler[24], P. Shchekaturov[2], M. Seidel[2], C. Soenke[2],
E. Stadler[1], C. Stephan[24], M. Suárez[2], M. Todorovic[2], G. Valdes[24], C. Verinaud[2],
G. Zins[2], and S. Zúñiga-Fernández[24,38,39]
(NAOMI Collaboration)

(Affiliations can be found after the references)

ABSTRACT

Context. Since 2019, GRAVITY has provided direct observations of giant planets and brown dwarfs at separations of down to 95 mas from the host star. Some of these observations have provided the first direct confirmation of companions previously detected by indirect techniques (astrometry and radial velocities).

Aims. We want to improve the observing strategy and data reduction in order to lower the inner working angle of GRAVITY in dual-field on-axis mode. We also want to determine the current limitations of the instrument when observing faint companions with separations in the 30–150 mas range.

Methods. To improve the inner working angle, we propose a fiber off-pointing strategy during the observations to maximize the ratio of companion-light-to-star-light coupling in the science fiber. We also tested a lower-order model for speckles to decouple the companion light from the star light. We then evaluated the detection limits of GRAVITY using planet injection and retrieval in representative archival data. We compare our results to theoretical expectations.

Results. We validate our observing and data-reduction strategy with on-sky observations; first in the context of brown dwarf follow-up on the auxiliary telescopes with HD 984 B, and second with the first confirmation of a substellar candidate around the star *Gaia* DR3 2728129004119806464. With synthetic companion injection, we demonstrate that the instrument can detect companions down to a contrast of 8×10^{-4} ($\Delta K = 7.7$ mag) at a separation of 35 mas, and a contrast of 3×10^{-5} ($\Delta K = 11$ mag) at 100 mas from a bright primary ($K < 6.5$), for 30 min exposure time.

Conclusions. With its inner working angle and astrometric precision, GRAVITY has a unique reach in direct observation parameter space. This study demonstrates the promising synergies between GRAVITY and *Gaia* for the confirmation and characterization of substellar companions.

Key words. techniques: high angular resolution – techniques: interferometric – planets and satellites: detection – brown dwarfs – planetary systems

1. Introduction

Thanks to progress in ground-based and space-based direct imaging instrumentation, we can now delve into the specific formation processes leading to substellar companions, such as massive planets and brown dwarfs. It has been proposed that they form by core accretion (Mizuno 1980), disk instability (Boss 1997), or collapse of the prestellar core (Bonnell et al. 2008), and all these models come with different variations. It is still unclear as to which mechanism dominates in each type of object and at what distance. Extensive direct imaging surveys (e.g., Vigan et al. 2021; Nielsen et al. 2019; Stone et al. 2018) have inferred the occurrence rates of massive Jovian planets and brown dwarfs around stars of spectral types from B to M. For intermediate FGK stars, the findings of these surveys favor a dichotomy in the formation processes. The distribution of giant planets within 50 au is consistent with the predictions of the core-accretion model, and the giant planet and brown dwarf populations further out are consistent with the disk-instability pathway. Also, by fitting the orbit of a sample of a dozen substellar companions, Bowler et al. (2020) revealed a difference in the eccentricity distribution of giant planets and brown dwarfs. These authors suggest that planets form in disks and brown dwarfs preferably by core collapse. The most promising way to enlarge the samples for testing the formation theories is to enable direct observations of fainter companions, and to reach the closer-in regions of the systems (below 20 au).

On the one hand, this goal of observing fainter companions at shorter separations triggers the development of faster and higher-order adaptive optics (AO) (Boccaletti et al. 2022; Lozi et al. 2022; GRAVITY+ Collaboration 2022) and deconvolution techniques in high-contrast images (e.g., angular differential imaging: Marois et al. 2006, spectral differential imaging: Racine et al. 1999). So far, ground-based AO-assisted single telescopes and space instruments achieve contrasts down to a few 10^{-7} at 1 arcsec separation (ERIS: Davies et al. 2023, SPHERE: Beuzit et al. 2019, GPI: Macintosh et al. 2014, HiRISE: Otten et al. 2021, KPIC: Jovanovic et al. 2019, JWST: Hinkley et al. 2022). On the other hand, optical long-baseline interferometry with GRAVITY is emerging as a complementary technique because its specific deconvolution capability allows direct observations of planetary companions at separations of as small as 90 mas.

GRAVITY is a second-generation K-band instrument and a two-in-one interferometric combiner in operation at the Very Large Telescope Interferometer (VLTI) since 2016 (GRAVITY Collaboration 2017). The fringe tracker (FT, Lacour et al. 2019) arm operates at 1 kHz on a bright target ($K < 10$) in order to adjust the delay-lines position and correct for atmospheric turbulence. In parallel, the science (SC) arm can integrate up to 300 s, and thus allows for observations of objects as faint as $K = 19$ mag (GRAVITY Collaboration 2022). In addition, a metrology system measures the angular separation between the FT and the SC in real time. The ability to observe faint objects, together with the robust metrology link between FT and SC, launched optical interferometry into the field of direct imaging of exoplanets. The ExoGRAVITY large program has already provided direct observations of exoplanets orbiting at 3 au from their stars, at challenging separations of down to 95 mas and contrasts of a few 10^{-5} (Nowak et al. 2020; Lacour et al. 2021; Hinkley et al. 2023). GRAVITY provides the relative astrometry with a precision down to 50 μas and a near-infrared K-band spectrometry at $R \sim 500$ (medium-resolution mode) or $R \sim 4000$ (high-resolution mode). These observations provide unprecedented constraints on the companion's orbit and allow determination of

the object's surface temperature and atmospheric composition (GRAVITY Collaboration 2020). However, the field of view of the instrument is limited due to the single-mode nature of modern optical interferometry. For more than 50% injection, it is about 65 mas on the unit telescopes (UTs) and 290 mas on the auxiliary telescopes (ATs). While this is an important drawback when performing blind searches, the situation has completely changed with the release of the *Gaia* space telescope catalog. *Gaia*'s Non-Single-Star (NSS) two-body orbit catalog (Holl et al. 2023; Halbwachs et al. 2023) published within DR3 (Gaia Collaboration 2023) contains astrometry-based orbital solutions for approximately 450 000 stars around each system's center of mass. Assuming that the orbital motion of the star is caused by the presence of a dark and unseen secondary body, the orbital solution constrains the on-sky position of the companion relative to the star with sufficient accuracy to position the single-mode fiber of GRAVITY. A subsequent detection of the companion with GRAVITY can confirm the candidate and provide the dynamical mass – thanks to the astrometry – and a direct measurement of its luminosity and spectrum. This synergy has been identified for a few years now, but there is currently no quantitative assessment of its potential. The actual inner working angle and contrast performance of GRAVITY are still undocumented, and their limitations are still unknown. These questions become even more pressing in the context of the ongoing instrumentation upgrade at the VLTI (Eisenhauer 2019).

The goal of this paper is to demonstrate and quantify the potential of GRAVITY to provide direct confirmations of substellar candidates detected by *Gaia* absolute astrometry and to understand its limitations. In Sect. 2, we describe specific details of substellar companion observations and data reduction with GRAVITY. We outline a strategy to lower the inner working angle. In Sect. 3, we quantify and validate these strategies by observing the brown dwarf HD 984 B and by providing the first direct observation of a brown dwarf companion orbiting the star *Gaia* DR3 2728129004119806464 (hereafter referred to as *Gaia*...6464). Finally, in Sect. 4, we determine the detection limits of GRAVITY by injection and retrieval of synthetic companions in archival ExoGRAVITY observations. We compare the results with expectations from the fundamental statistical noise. We conclude the paper with a summary and a discussion of the synergy with *Gaia* and other direct-imaging instruments (Sect. 5).

2. Method

2.1. The ExoGRAVITY method

The ExoGRAVITY community developed an observation technique and a dedicated pipeline to enable direct observations of exoplanets and brown dwarfs with the GRAVITY instrument down to a few tens of mas close to bright nearby stars (Nowak et al. 2020; GRAVITY Collaboration 2020).

2.1.1. Observing technique

The VLTI recombines either the four relocatable ATs, each of $D = 1.8$ m in diameter, or the four UTs, each of $D = 8$ m in diameter. The beam from each telescope travels through the VLTI tunnels and delay lines to reach GRAVITY. In the instrument, the two combiners (FT and SC) are fed by separate optical single-mode fibers. In the dual-field mode of the instrument, the fibers of the SC and of the FT can be positioned at different locations on the focal plane of each telescope (Pfuhl et al. 2012).

For separations of less than 0.7 arcsec, the field is separated by a 50/50 beamsplitter before injection into the FT and SC fibers (Appendix A in Nowak et al. 2020). In a typical ExoGRAVITY observation sequence, the FT remains centered on the host star and the SC alternates between long integrations centered on the companion and shorter integrations centered on the star (to avoid saturation). The shape of the fiber mode can be approximated by a Gaussian beam with a full width at half maximum (FWHM) of 65 mas on the UT (290 mas on the AT), which defines the field of view of the instrument. The flux injected into the SC from individual telescopes is recombined in integrated optics (Perraut et al. 2018). The recombination method allows us to measure the total flux of each of the four telescopes, but also the coherent flux of each of the six baselines.

Regarding the total flux (e.g., photometric flux of each telescope), the injected flux is the scalar product between the Gaussian mode of the fiber and the object point-spread function (PSF; Fig. 1). The dependence of the transmission on the distance **s** of the object from the center of the fiber is thus given by

$$T(m, \mathbf{s}) = \left| \iint E(\mathbf{x}, m) \, M(\mathbf{x} - \mathbf{s}) \, d\mathbf{x} \right|^2, \quad (1)$$

where m is the telescope, E the incident electric field, M the fiber mode, and $\mathbf{x} = (x, y)$ the coordinates on the focal plane. In the following, we consider that T includes the overall transmission from the atmosphere and the instrument; it therefore depends on the telescope, time, and wavelength. This way, the total flux $F_{\text{oncompanion}}$ injected into the SC for each of the four telescopes when the fiber is centered on the companion can be expressed as

$$F_{\text{oncompanion}}(m, t, \lambda)$$
$$= F_s(\lambda) \, T(m, \Delta\boldsymbol{\alpha}, t, \lambda) + F_c(\lambda) \, T(m, \mathbf{0}, t, \lambda), \quad (2)$$

where m is the telescope, t the time, λ the wavelength, $\Delta\boldsymbol{\alpha} = (\Delta\text{RA}, \Delta\text{Dec})$ the position of the companion relative to the star, and F_s and F_c are the total flux from the star and the companion, respectively.

The coherent flux, also called the complex visibility, encodes the amplitude and the phase of the interferometric fringes and provides the useful signal in GRAVITY. We can define the interferometric transmission G as:

$$G(b, \mathbf{s})$$
$$= \iint E(\mathbf{x}, m_1) \, M(\mathbf{x} - \mathbf{s}) \, d\mathbf{x} \cdot \iint E^*(\mathbf{x}, m_2) M^*(\mathbf{x} - \mathbf{s}) \, d\mathbf{x}, \quad (3)$$

with the two telescopes m_1 and m_2 composing the baseline b. We can then write the complex visibility $V_{\text{oncompanion}}$ that the instrument measures when the SC fiber is located on the companion as

$$V_{\text{oncompanion}}(b, t, \lambda)$$
$$= V_s(b, t, \lambda) \, G(b, \Delta\boldsymbol{\alpha}, t, \lambda) + V_c(b, t, \lambda) \, G(b, \mathbf{0}, t, \lambda), \quad (4)$$

where V_s and V_c are the visibility of the star and the companion, respectively. Here and in the following, the visibility is understood as the complex coherent flux, which matches the definition of Nowak et al. (2020).

The total transmission T and the interferometric transmission G include the flux losses due to the distance of the fiber from the object (star or companion). We estimated the dependence of
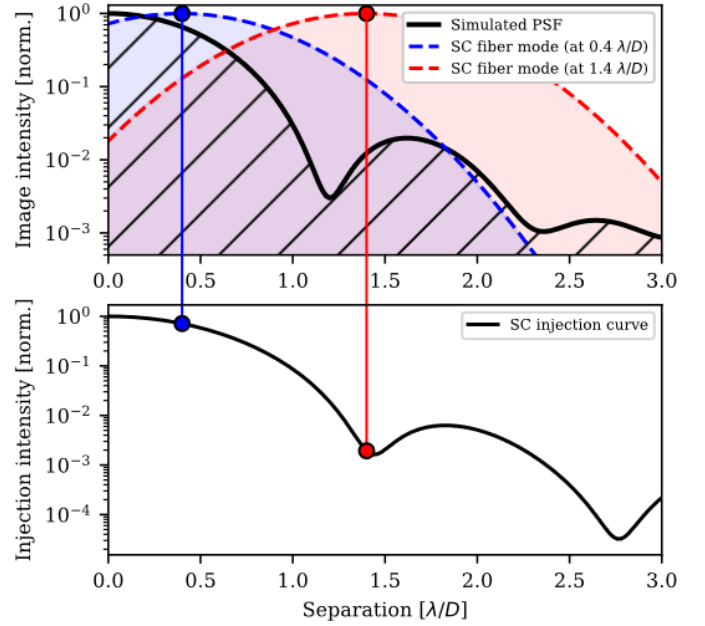

Fig. 1. Injection into the SC arm at the focal plane of GRAVITY. Top: comparison of the Gaussian single mode of the SC fiber with the diffraction-limited PSF at the image plane. This simulation is for 20% bandwidth and the UT aperture. Bottom: injection map given by the convolution of the PSF with the SC fiber mode.

the transmission on separation using archival observations from the ExoGRAVITY large program 1104.C-0651(A). We selected observations with good atmospheric conditions. In the selected observations, the companion is fainter than contrasts of 10^{-4}, and so the total flux $F_{\text{oncompanion}}$ and the coherent flux $V_{\text{oncompanion}}$ are largely dominated by the star contribution and we neglect the companion contribution. The GRAVITY pipeline (Lapeyrere et al. 2014) outputs an ASTROREDUCED file containing the total flux per telescope and per detector exposure (OI_FLUX table) and the coherent flux per baseline and per detector exposure (OI_VIS table). The ExoGRAVITY pipeline reads these files and normalizes the fluxes measured on-companion by the fluxes measured on-star. Therefore, the output immediately corresponds to the normalized injection curve.

Figure 2 displays the normalized coherent and total fluxes measured at different separations. These are based on archival observations from the ExoGRAVITY large program around bright stars from $K = 7.5$ mag to $K = 3.5$ mag (β Pic, HD 206893, HD 17155, and CD-50 869). This dataset covers SC fiber positions from 55 to 140 mas, and atmosphere conditions from good to normal (seeing from 0.4 to 1.0 arcsec). To obtain continuous injection profiles, we ran AO simulations including single-mode fiber injection with HCIPy (Por et al. 2018). We simulate an atmosphere following Kolmogorov turbulence and a low-order AO controlling 50 modes over an 8 m pupil to mimic the MACAO system at the Coudé focus of the UT (Arsenault et al. 2003). We include 20% bandwidth to account for the spectral range of GRAVITY from 1.95 to 2.4 µm. We also add realistic 10 mas rms tip-tilt jitter residuals from the VLTI tunnels (Anugu et al. 2018). Finally, we adjust the AO loop gain and atmosphere parameters to match the observed total fluxes (coherent and total). The total flux transmission T and the interferometric transmission G are not at the diffraction limit level because of atmospheric residuals not corrected for by the AO, turbulence in the VLTI tunnels, and (quasi-)static aberrations in the instrument. The simulations show that the average Strehl
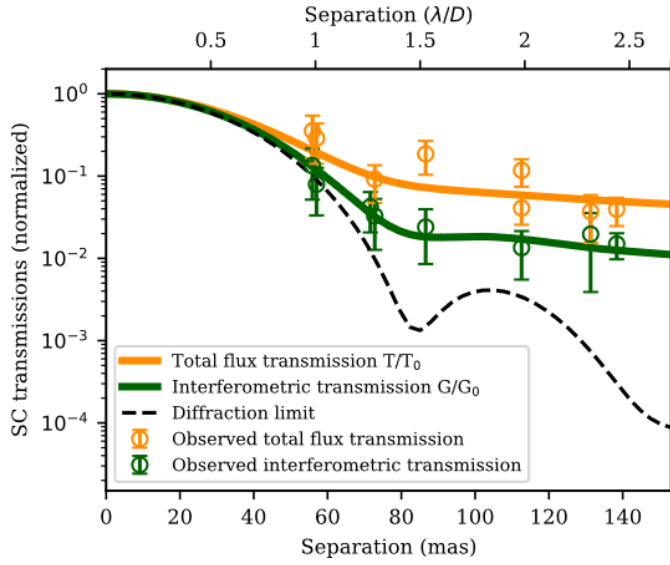
Fig. 2. Total flux transmission (T) and interferometric transmission (G) as a function of the separation from the star on the UT. The points correspond to archival ExoGRAVITY observations around bright stars. The solid lines correspond to simulations matching the observations. The dashed line corresponds to a simulation of the transmission without atmospheric residuals but including a 20% bandwidth and 10 mas rms tip-tilt jitter.

ratio in ExoGRAVITY observations is around 25%, which is a realistic value. In the remainder of the paper, we use the continuous profiles to model the injection of coherent and total flux in GRAVITY.

2.1.2. Unveiling the companion signal

The goal of the ExoGRAVITY reduction pipeline is to extract the companion astrometry and contrast spectrum from the measured complex visibilities $V_{\mathrm{oncompanion}}(b, t, \lambda)$. In the following, "speckle" refers to the flux of the star that couples in the SC combiner while observing the companion. As shown in Eqs. (2) and (4) and in Fig. 2, this speckle light makes a contribution to the total flux, but also to the coherent flux. It is necessary to deconvolve the companion signal (coherent flux) from the coherent speckles. The companion is modeled as a point-source offset with respect to the host star. The complex visibility of the companion is:

$$V_{\mathrm{c}}(b, t, \lambda) = S_{\mathrm{c}}(\lambda)\, e^{-i\frac{2\pi}{\lambda}[\mathbf{u}(t)\Delta\boldsymbol{\alpha}]}, \tag{5}$$

where S_{c} is the companion spectrum and $\mathbf{u} = (u, v)$ the coordinates of the array on the UV plane. In the ExoGRAVITY pipeline, the speckle term $V_{\mathrm{s}}G$ of Eq. (4) is modeled as

$$V_{\mathrm{s}}(b, t, \lambda)\, G(b, \Delta\boldsymbol{\alpha}, t, \lambda) = P(b, t, \lambda)\, V_{\mathrm{onstar}}(b, t, \lambda), \tag{6}$$

where P is a complex polynomial that captures the spectral dependence of the coupling G at the separation $\Delta\boldsymbol{\alpha}$, and V_{onstar} is the visibility measured with the SC fiber centered on the host star:

$$V_{\mathrm{onstar}} = J(b, t, \lambda)\, G(b, \mathbf{0}, t, \lambda)\, S_{\mathrm{s}}(\lambda). \tag{7}$$

Here, S_{s} is the star's spectrum, and J is the function representing the drop in the visibility of the star if the star is resolved by the

interferometer. In the following, we assume that the star is not resolved, and so $J = 1$. Introducing the contrast spectrum

$$C(\lambda) = S_{\mathrm{c}}(\lambda)/S_{\mathrm{s}}(\lambda), \tag{8}$$

we can rewrite Eq. (4) phase referenced on the star:

$$V_{\mathrm{oncompanion}}(b, t, \lambda) = P(b, t, \lambda)V_{\mathrm{onstar}} + C(\lambda)V_{\mathrm{onstar}}e^{-i\frac{2\pi}{\lambda}\cdot[\mathbf{u}(t)\Delta\boldsymbol{\alpha}]}. \tag{9}$$

The first pass through the algorithm requires an assumption on $C(\lambda)$, and so, as a first guess, we assume that $C(\lambda)$ is a flat contrast spectrum. This first pass allows the recovery of the companion astrometry and the average flux ratio, and is the focus of this work. The second part of the pipeline (not described here) uses the astrometry to recover the companion contrast spectrum.

Equation (9) demonstrates the distinction between the speckle signal (first term) and the companion signal (second term). On the one hand, the speckle signal modulates at low spectral frequencies. On the other hand, the companion signal modulates at spectral frequencies that are determined by the projection of the companion separation onto the UV plane. This difference in the spectral oscillations allows the star light to be disentangled from the companion light (see Appendix A for an example). This is the interferometric equivalent of the "spectral deconvolution" first introduced by Sparks & Ford (2002) for high-contrast imaging with single telescopes.

2.2. Aiming for a smaller inner working angle

The previous section describes the standard ExoGRAVITY method. We now describe two modifications designed to improve the inner working angle.

2.2.1. Off-pointing strategy

Figure 2 indicates that it should be possible to improve the flux ratio between the companion and the star by offsetting the position of the fiber when observing the companion. This adds a new degree of freedom in the observation: the offset $\boldsymbol{\delta}$ of the SC fiber with respect to the expected companion position. This way, Eqs. (2) and (4) can be rewritten as

$$F_{\mathrm{oncompanion}}(m, t, \lambda)$$
$$= F_{\mathrm{s}}(\lambda)\, T(m, t, \Delta\boldsymbol{\alpha} + \boldsymbol{\delta}, \lambda) + F_{\mathrm{c}}(\lambda)\, T(m, t, \boldsymbol{\delta}, \lambda), \tag{10}$$
$$V_{\mathrm{oncompanion}}(b, t, \lambda)$$
$$= V_{\mathrm{s}}(b, t, \lambda)\, G(b, t, \Delta\boldsymbol{\alpha} + \boldsymbol{\delta}, \lambda) + V_{\mathrm{c}}(b, t, \lambda)\, G(b, t, \boldsymbol{\delta}, \lambda). \tag{11}$$

To reduce the star light without excessively reducing the coupling of the companion light, the offset $\boldsymbol{\delta}$ must be in the direction away from the star and of only a fraction of the PSF central lobe width. The off-pointing technique takes advantage of the sharp decrease in stellar transmission and the moderate decrease in companion transmission when the fiber is moved away from the star by a small offset $\boldsymbol{\delta}$.

2.2.2. Order of the polynomial fit

Section 2.1.2 implies that the degree of the polynomial P used to reject the speckles determines the inner working angle of the ExoGRAVITY technique. There is a trade-off between the quality of the speckle fit, and the self-subtraction of the planet

signal. This is common to most deconvolution techniques. By default, the ExoGRAVITY pipeline uses a fourth-degree polynomial for P. This has proven necessary to deal with the frequent fringe jumps of the fringe tracker. Such phase jumps cause a loss of visibility at the edges of the K-band visibility spectrum. These visibility losses are not necessarily of the same amplitude when observing on the star and on the planet, depending on the non-stationary quality of the fringe tracking. A fourth-degree polynomial is required to capture and remove these features. Consequently, most results published so far with the ExoGRAVITY pipeline have used a polynomial of between fourth and sixth order.

However, the situation recently changed with the commissioning of an improved version of the fringe tracker hardware and tracking algorithm in November 2022 (Abuter et al. 2016; Nowak et al. 2024). The new FT update significantly reduces the occurrence of fringe jumps and thus relaxes the requirements on the degree of the polynomial. It is also interesting to explore the impact of this parameter because the planned upgrade of the AO will stabilize the Strehl, and thus further reduce the occurrence of fringe jumps.

2.3. Empirical detection limit

The standard ExoGRAVITY pipeline lacks a method for determining robust detection limits. The injection of synthetic companions and their retrieval in the data is a classical approach to assessing the limit of direct imaging techniques in realistic conditions. The first step is to create a data set without a companion signal (if the original observation contains one). For this, we extract the companion astrometry ΔRA, ΔDec and the contrast spectrum $C(\lambda)$ exposure by exposure thanks using the ExoGRAVITY pipeline (Sect. 2.1.2). We then subtract the signal of this companion in the VISDATA table of the ASTROREDUCED files. We note that, unlike most other interferometric instruments, this operation is linear because GRAVITY operates with first-order estimators (complex coherent flux) instead of higher-order estimators (power spectrum and bispectrum). We then add synthetic companions at a given contrast C and $\Delta\alpha$ position to the VISDATA:

$$V_{\mathrm{syntheticcomp}} = C \, V_{\mathrm{onstar}} \, e^{-i\frac{2\pi}{\lambda} [\mathbf{u}(t)\Delta\alpha]} \, e^{i\varphi}. \tag{12}$$

The additional φ phase term is due to the fact that the complex visibilities VISDATA are phased on the fiber position, and that the phase reference is the fringe-tracking phase, which is not necessarily zero. The term φ writes:

$$\varphi = arg(\mathrm{STAR\_REF}) - \mathrm{PHASE\_REF} \tag{13}$$
$$+ \mathrm{PHASE\_MET} + \frac{2\pi}{\lambda}\mathrm{DISP},$$

following the nomenclature of the GRAVITY pipeline user manual[1], where PHASE_REF is the phase of the fringe tracker, PHASE_MET the differential phase between the fiber coupler and telescope diodes, DISP the fiber differential delay lines (FDDL) delay, and STAR_REF is the average of the two closest acquisitions with the SC on-star. In Eq. (13), we use a STAR_REF expression that has been previously rephrased with the metrology (PHASE_MET) and FDDL delay (DISP). In this paper, we inject companions with a flat contrast spectrum for the

---

[1] https://www.eso.org/sci/software/pipelines/index.html#pipelines_table
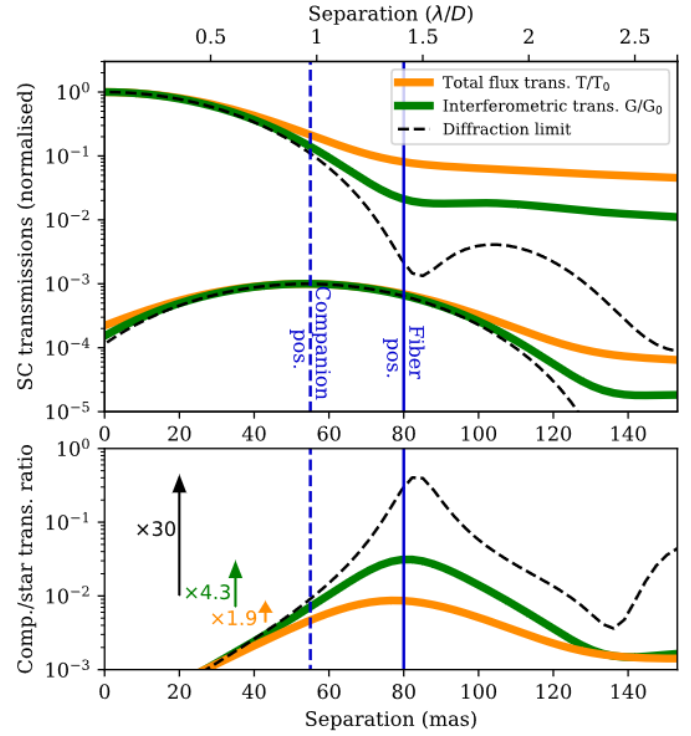

Fig. 3. Quantification of the contrast improvement brought by the off-pointing strategy in the case of a companion at a separation of 55 mas. Top: dependence on separation of both transmission of the total flux (T) and interferometric transmission (G) for a star and a companion. The diffraction limit represents an ideal unaberrated case. Bottom: companion-to-star transmission ratio with respect to separation. The arrows indicate the gain in contrast with a +25 mas SC fiber offset.

sake of simplicity, and so C is scalar. The modified VISDATA are then reduced by the ExoGRAVITY pipeline.

We consider the detection successful if the companion is recovered less than 3 mas away from the injected position and at a contrast with less than 50% relative error compared to the injected contrast. We consider that the detection limit is reached when fewer than 68% (1σ) of the synthetic companions are successfully retrieved.

3. Results

3.1. Expected performance improvement

3.1.1. Off-pointing technique

We use the injection profiles shown in Fig. 2 to quantify the improvement that can be achieved by the off-pointing technique. Figure 3 shows that an offset of the fiber position can result in a factor 4.3 improvement in the companion/star coherent flux ratio and a factor 1.9 improvement of the total flux ratio. In this example, the companion is at 55 mas from the host star, and the fiber is positioned at 80 mas (55 mas + 25 mas away from the star). The fiber offset from the companion results in an injection efficiency of 67% (it would be 100% if the fiber were centered on the companion). This flux loss due to the offset must be compensated for a posteriori in order to recover the correct companion magnitude (Wang et al. 2021b; Appendix A). We estimate that, with the current AO on the UT, this method can bring a contrast enhancement in coherent flux of up to a factor 6. In terms of the implementation, for companions with a separation of less
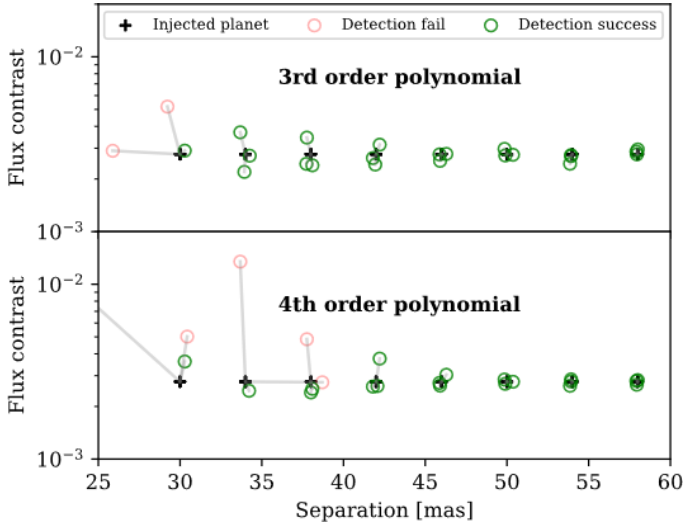
Fig. 4. Planet retrieval at 2.7×10^{-3} raw contrast and separations from 30 to 90 mas. At each separation, three companions are injected at different positional angles to test the robustness of the retrieval. We compare the third-degree (top) and fourth-degree (bottom) polynomials for speckle modeling.

than 55 mas, the SC fiber should be placed at +25 mas from the companion, because a higher offset would result in more planet flux loss and possible errors in the astrometry due to aberrations in the fiber injection (GRAVITY Collaboration 2021). For companions with a separation of between 55 mas and 80 mas, the SC fiber should be placed at 80 mas from the star. The offset method is not valid for companions with separations of greater than 80 mas, and so the SC fiber should be placed on the companion for these targets.

The improvement provided by the off-pointing strategy is currently severely limited by the AO performance. The dashed curve in Fig. 3 represents a realistic improved version of VLTI, with a high-order AO and control of the instrument aberrations. The expected injection profile was computed with the diffraction limit plus a 10 mas tip-tilt jitter, for instance resulting from the VLTI tunnels. The curve also considers a 20% wavelength bandwidth. Under these conditions, off-pointing can bring a contrast enhancement of up to a factor 30. This result emphasizes the need for better AO and instrument aberration control, as will be implemented with GRAVITY+.

3.1.2. Order of the polynomial fit

We used the planet injection and retrieval method described in Sect. 2.3 to define the most relevant polynomial degree when observing at short separation. We injected planets in the data set from the *Gaia*...6464 B run on the UT with the SC fiber at 60 mas of the primary (described in detail in Sect. 3.3). We then determined the best polynomial order to use in the reduction depending on the expected separation of the companion.

Figure 4 compares the performance of the third- and fourth-order polynomials for speckle modeling. The third-order polynomial leads to better planet retrieval below 45 mas separation, for both position and contrast. Beyond 45 mas, the fourth-order polynomial gives slightly better results for contrast retrieval. For completeness, we also ran tests with second-order polynomials. In this case, the retrieval gives erratic results. Thus, we still consider it safer to use the fourth order for separations of greater than

Table 1. Log for the GRAVITY observations of HD 984 AB on the AT.

	Date: 2022-10-24		
Observing time	Airmass	$\tau_0{}^{(a)}$	Seeing
01:12:17/01:57:20	1.07–1.14	2.5–4.5 ms	0.43–0.66″
Target	ΔRA/ΔDec$^{(b)}$	NEXP/NDIT/DIT	
HD 984 A	0/0 mas	2/8/10 s	
HD 984 B	162/197 mas	3/8/30 s	
HD 984 B	224/273 mas	3/8/30 s	

Notes. $^{(a)}$Atmosphere coherence time. $^{(b)}$SC fiber position relative to the star.

45 mas, as it gives more degrees of freedom for speckle modeling; nevertheless, we recommend using a third-order polynomial below 45 mas separation. This improvement brings the effective innermost working angle of GRAVITY to about 30 mas.

3.2. On-sky validation on the auxiliary telescopes

3.2.1. Observation and data reduction

The star HD 984 A is known to host a companion brown dwarf with a contrast at K-band of 3.7×10^{-3} (Meshkat et al. 2015; Franson et al. 2022). We used this binary system to validate the off-pointing technique described in Sect. 2.2.1. The observation was performed as part of the program 0110.C-0182(A), on the ATs in astrometric configuration, and with the medium spectral resolution of GRAVITY. The off-pointing technique described for the UT is still valid on the AT, but since the ATs are smaller, it requires a ×4.4 scaling on the angular separations. From orbit fits using previous observations (Wang et al. 2021a), the companion was expected at a separation of 255 mas, with ±5 mas uncertainty on the (ΔRA, ΔDec). During the observation, the SC fiber was alternately positioned on the predicted position of the companion and 100 mas further away from the star (+0.4 λ/D), as summarized in Table 1. We chose a detector integration time (DIT) of 30 s, we collected a number of acquisition (NDIT) equal to eight in each of the three files (NEXP), and this for each position of the SC. We reduced the data using the ExoGRAVITY pipeline. The data taken with and without the off-pointing technique were reduced separately to compare the results. After reduction, it appeared that the companion was 9 mas away from the expected position. As this corresponds to only 3% of the fiber field of view on the AT, it did not entail flux losses and had no negative effect on our test.

3.2.2. Contrast improvement

Applying the offset on the fiber position, the coherent flux injected into the SC is reduced by a factor 6 and the total flux is reduced by a factor 3.4 on average. The slightly better improvement compared to expectations (factor 4 in coherent flux) is because the NAOMI AO on the ATs (Woillez et al. 2019) are closer to the diffraction limit than the UT with MACAO. The off-companion observations provide a significantly better detection than the on-companion, with about twice the periodogram power, from 1.4×10^4 to 2.7×10^4, as shown in Fig. 5.

Relative astrometry is improved by the off-pointing technique. With the off-pointing observation, the uncertainty on the ΔRA is reduced by 35% and the uncertainty on ΔDec is reduced by 8% compared to the classical on-companion pointing.
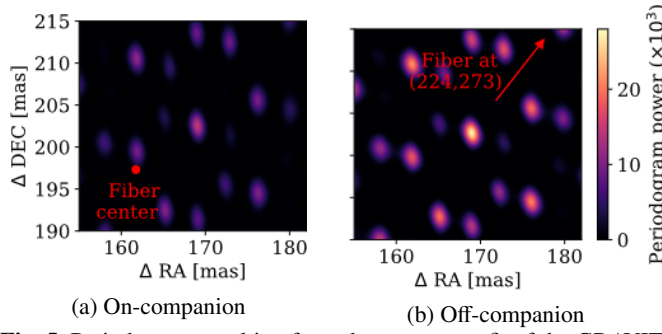
Fig. 5. Periodogram resulting from the astrometry fit of the GRAVITY data on HD 984 obtained by pointing the fiber at the expected position of the companion (left) and using the off-pointing technique (right). The spot of higher periodogram power corresponds to the detection of HD 984 B.
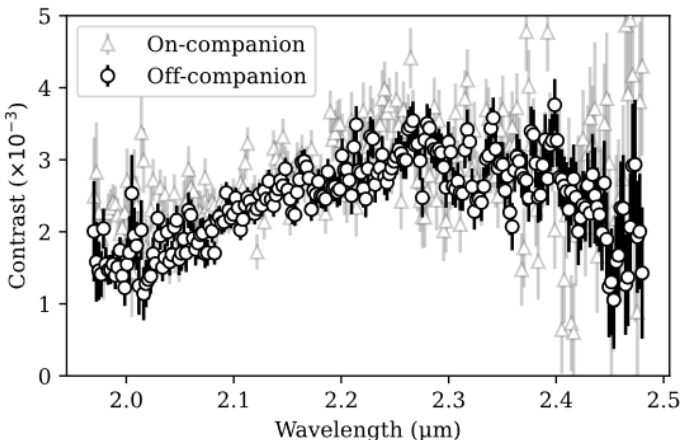

Fig. 6. Contrast spectrum for HD 984 B from our observations with (black) and without (gray) the off-pointing technique.

We also ran the second part of the pipeline to obtain the contrast spectrum. The spectrum quality is expected to improve thanks to the off-pointing. On the one hand, with the reduction of the total flux, we expect the amplitude of the photon noise from star speckles to be reduced by a factor of 1.8. On the other hand, only 72% of the companion flux is injected due to the off-pointing. Overall, we expect an improvement of 30% of the spectrum signal-to-noise ratio (S/N). The resulting contrast spectra are shown in Fig. 6. The total S/N can be calculated as:

$$S/N = \sqrt{C^{\intercal}.\mathrm{COV}^{-1}.C,} \tag{14}$$

where C is the contrast spectrum, $C^{\intercal}$ its vector transpose, and COV is the covariance matrix of the spectrum. The S/N is equal to 120 for the on-companion observations and is equal to 164 (+37%) for the off-companion data. This is fully in line with expectations.

3.2.3. Discussion

The efficiency of the interferometric deconvolution depends on the length of the baselines and the separation. In other words, a companion at 1 $\lambda/D = 252$ mas separation on the ATs is easier to disentangle from the speckles than a companion at 1 $\lambda/D = 57$ mas on the UTs. Nevertheless, this observation of HD 984 B with the AT demonstrates that a +0.4 λ/D offset brings a significant reduction of the coherent and total stellar flux, a better
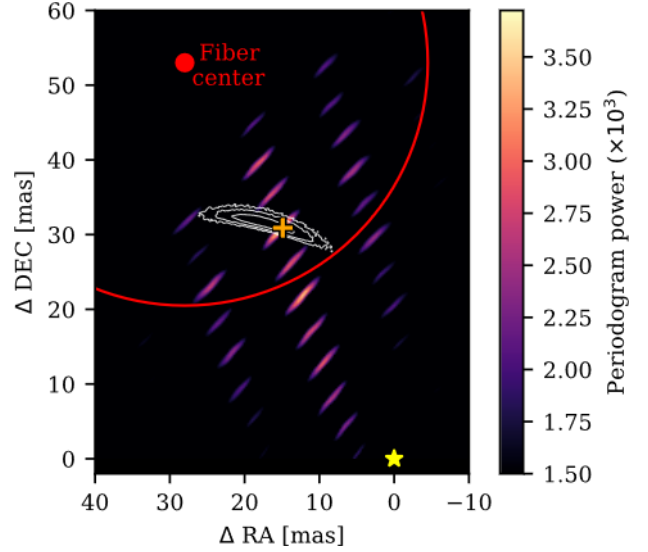

Fig. 7. Periodogram from the astrometry fit of the observations of *Gaia*...6464 B. The best-fit position of the *Gaia*...6464 B according to the ExoGRAVITY pipeline is indicated by the orange plus symbol. The position of the primary star is marked by the yellow symbol. The white contour lines are the *Gaia*-based position probability density of the dark companion (from inside to outside: 68, 95, and 99.7 % of the total set of position predictions). The position of the SC fiber in the field is given by the red dot, while the fiber field of view (50% flux injection limit) is shown by the red circle.

detection, and a higher S/N spectrum. It also shows that the technique does not introduce significant astrometric errors.

3.3. Application to Gaia... 6464 B on the unit telescopes

We compiled a list of objects from the *Gaia* NSS catalog with candidate substellar companions that are accessible for direct confirmation with GRAVITY (Winterhalder et al. 2024). As a proof of concept, we observed the candidate *Gaia*...6464 with the UTs during a technical time request for the science verification of a GRAVITY FT upgrade (60.A-9102).

3.3.1. Observations and data reduction

We predict the position of *Gaia*...6464 B from the NSS catalog orbital solution, assuming that the companion does not contribute to the flux observed in the *G*-band and that the companion mass is the lower estimate listed in the *Gaia* DR3 `binary_masses` table. We use a randomization procedure to obtain the projected position probability shown in Fig. 7. The companion position is predicted with ±5 mas uncertainty on separation, and ±8° uncertainty on positional angle at 1σ. Given the short predicted separation for the companion (close to 35 mas), we pointed the science fiber 25 mas away from the predicted position to reduce the host star flux injection, as described in Sect. 2.2.1. GRAVITY was set to medium spectral resolution and we used the dual-field on-axis mode. A detailed summary of the observing conditions and exposure time settings can be found in Table 2.

We applied the standard ExoGRAVITY pipeline, except that we reduced the polynomial order to 3 for the speckle fit, as described in Sect. 2.2.2. Figure 7 shows the resulting periodogram. *Gaia*...6464 B is detected at a separation of 34 mas and

Table 2. Log for the GRAVITY observations on the unit telescopes.

	Date: 2022-11-09		
Observing time	Airmass	τ_0	Seeing
01:51:09/02:57:59	1.54–2.16	3.5–9.6 ms	0.35–0.88″
Target	ΔRA/ΔDec[a]	NEXP/NDIT/DIT	
Gaia...6464 A	0/0 mas	4/12/10 s	
Gaia...6464 B	28/53 mas	16/4/30 s	

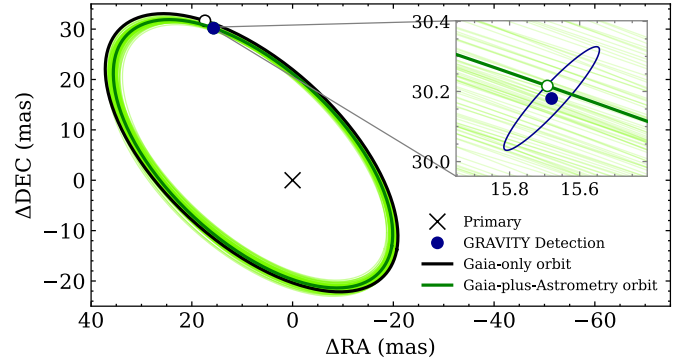**Notes.** [a]SC fiber position relative to the star.

Fig. 8. Orbit of the companion *Gaia*...6464 B. The original *Gaia* orbit is shown in black. The refined orbit resulting from the combination of the *Gaia* solution and the astrometric position measurement provided by GRAVITY is shown in dark green. The light green shows a random subset of the sampled solutions probed during the MCMC run. The blue dot indicates the GRAVITY measurement with the ellipse describing the associated uncertainty. On the main plot, the black circle shows the position of the companion at the time of the observation as predicted by the *Gaia*-only orbital solution. On the inner plot, the green circle shows the position of the companion from the refined orbital solution including the GRAVITY observation.

2.5 mas from the predicted position. The contrast at *K*-band, corrected for fiber injection loss, is $(3.1 \pm 0.5) \times 10^{-3}$. We confirmed the detection by injecting and recovering synthetic companions in the data at similar contrasts, as described in Sect. 2.3. All the injected companions were correctly retrieved by the pipeline.

3.3.2. Dynamical mass determination

The use of the fiber off-pointing and the lower-order polynomial for speckle fitting allowed a direct observation of *Gaia*...6464 B at the innermost separations possible with the ExoGRAVITY technique. This detection can be used to infer the dynamical masses of the companion and primary, and to further constrain the orbital solution presented in the *Gaia* NSS catalog. To this end, we require two pieces of information from the GRAVITY direct imaging: confirmation of the dark companion hypothesis and the precise relative astrometry.

We used a Markov Chain Monte Carlo (MCMC) framework based on Foreman-Mackey et al. (2013) to combine *Gaia* and GRAVITY data. It should be noted that *Gaia* NSS data must be handled with care when used in combination with MCMC methods, especially for low-eccentricity orbits (Babusiaux et al. 2023). We used BINARYS (Leclerc et al. 2023) to confirm that our MCMC analysis of *Gaia*...6464 B is well-behaved and gives results similar to the those obtained with the local linear approximation technique.

The direct observation provides the companion-to-star flux ratio, which is crucial for mass determination. We compared the mass results under two different assumptions: either the photocenter observed by *Gaia* is fully coincident with the primary position (dark-companion assumption), or the companion-to-primary flux ratio in the *Gaia* band in the visible is the same as the flux ratio measured at *K* band (faint-companion assumption). We find a companion mass that is $2\,M_{\mathrm{Jup}}$ higher under the faint-companion assumption and comparable error bars of the order of $3\,M_{\mathrm{Jup}}$ under the two assumptions. As the two hypotheses give similar results, and given that the flux ratio in the *G* band is expected to be lower than in the *K* band, the following orbital fit and mass determination remain under the dark-companion assumption.

The MCMC-based combination of observations from *Gaia* and GRAVITY results in an updated set of posterior distributions. In a Bayesian sense, these updated posteriors correspond to a more accurate description of the system, unless the *Gaia* and GRAVITY data conflict in some significant way. The initial and updated orbital solutions projected onto the sky plane are shown in Fig. 8. The *Gaia*-only solution is derived from the NSS catalog, and uses the primary mass derived by isochrone fitting (listed in the *Gaia* DR3 `binary_masses` table). The *Gaia*-only orbit also assumes the lower-limit mass ratio between

companion and host. As expected, the *Gaia*-only orbit and the *Gaia*+GRAVITY orbit are in good agreement. While the *Gaia* astrometry alone cannot constrain the individual masses, it is striking that a single observation with GRAVITY is sufficient to narrowly constrain the mass of the companion and the primary. We obtain $M_1 = 0.53^{+0.02}_{-0.02}\,M_{\odot}$ and $M_2 = 78.34^{+2.62}_{-2.50}\,M_{\mathrm{Jup}}$. The detected companion sits at the upper limit of the conventional mass range of brown dwarfs (13 to $80\,M_{\mathrm{Jup}}$). A detailed description of the method, along with the study of this companion and other targets are presented in Winterhalder et al. (2024).

4. Detection limits

Evaluation of the instrumental limits of detection is necessary in order to properly use nondetections in a statistically significant manner. Such an evaluation also allows the instrument to be placed in the larger instrumental landscape. This information is not yet available in the literature for GRAVITY. The goal of this section is to provide quantitative numbers on this question. Furthermore, this work allows us to comment on the possible nature of the noise process that limits the achievable contrast.

4.1. Contrast curves

We used the injection and retrieval technique described in Sect. 2.3. The data set consists of five archival ExoGRAVITY observations on the UTs (details in Appendix B) with the position of the SC fiber ranging from 54 to 136 mas. Archival observations are selected based on the criteria of having a bright primary ($K < 6.5$) and good atmospheric conditions (seeing <0.85 arcsec). The integration time for all observations is $5 \times 32 \times 10$ s (27 min) spread over 1 h to take advantage of the rotation of the UV plane. We simulated the fiber off-pointing technique below 80 mas separation (Sect. 2.2.1) by injecting the synthetic companion not at the fiber separation but closer to the host star. The retrieval process is computationally intensive, and so we limited the number of companions injected to five per separation and contrast. The five different injections were

performed at different positional angles to shuffle the possible effects of individual interferometric speckles in the observations. The separation of the injected companions is chosen in a range of maximum ±25 mas around the position of the SC fiber (see Table B.1). The ability to detect companions is significantly affected by the positional angle of the star companion with respect to the UV plane. Therefore, in the following study, we chose the positional angles for planet injection based on the orientation of the VLTI baselines and not on the positional angle of the SC fiber. We tested companion retrieval at the most optimal angle (i.e., parallel to the longest baselines on the UV plane) and at the least optimal angle (i.e., perpendicular to the longest baselines). After the companion injection, we ran the ExoGRAVITY pipeline to retrieve the companion signal. We average the signal from the 32 NDITs of individual exposures before reduction (fast mode of the ExoGRAVITY pipeline) in order to perform hundreds of injections and retrievals within a reasonable time frame.

The results are shown in Fig. 9. The contrast curve is obtained at 1σ when fewer than four out of the five companions are retrieved at the separation and contrast investigated. We cannot significantly determine 2σ or 3σ limits because of the limited number of companions injected. When the positional angle is parallel to the longest VLTI baselines, the sudden loss of sensitivity between 40 and 50 mas is due to the subtraction of the companion signal by the polynomial (Sect. 2.2.2). At separations of greater than 90 mas, the detection limit reaches 3×10^{-5} contrast ($\Delta K = 11.3$ mag). When the positional angle is perpendicular to the longest VLTI baselines, the contrast limit below 70 mas is ten times shallower than in the best position-angle case. The relative orientation must be considered when planning an observation. Beyond 130 mas separations, the contrast limit reaches 3×10^{-5} and the UV plane orientation no longer has any influence.

Finally, we explored the performance at larger separations. To this end, we performed additional injection and retrieval tests at 320 mas separation on AF Leporis b observations. The detection limit is at a contrast of 5.1×10^{-6} ($\Delta K = 13.2$ mag).

4.2. Empirical analysis of limitations

Detection on GRAVITY can be limited by either correlated noise or statistical noise in the measured visibilities. Correlated noise can be caused by stellar speckles that are not correctly fitted by the polynomial modeling. White noise is due to photon noise and detector noise.

We investigated the detection limit for different observing times using archive observations on the UT on HD 206893 (with the fiber at 111 mas separation) and β Pictoris (with the fiber at 92 mas separation). Both data sets have excellent atmospheric conditions and are bright enough for the AO to operate at the nominal regime. The HD 206893 data set has an exposure time of $27 \times 32 \times 10$ s (2.4 h) and spans over 3.5 h. The β Pictoris data set has an exposure time of $13 \times 32 \times 10$ s (1.2 h) and spans over 2.2 h. We select successive exposures in the data set to mimic a shorter observation time.

The results are summarized in Fig. 10. The evolution of the limit contrast roughly follows the inverse square root of the integration time. However, β Pictoris is seven times brighter in K-band than HD 206893. If limited by the photon noise of stellar flux leaking into the SC fiber, we expect the contrast to be $\sqrt{7} \approx 2.6$ deeper on β Pictoris than on HD 206893 at the same

(a) Best UV plane orientation
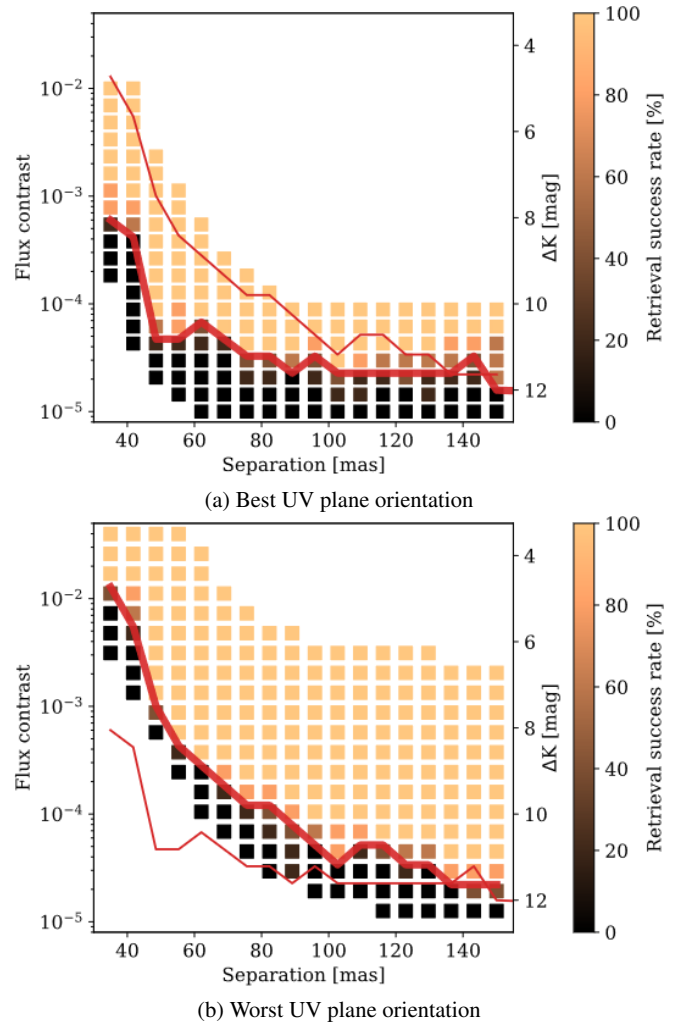

(b) Worst UV plane orientation

Fig. 9. Rates for successful retrieval of injected companions in Exo-GRAVITY observations with 10 s DIT and 27 min exposure time on the UT. (a) Retrieval when the star–companion couple is oriented in the direction of the longest VLTI baselines. (b) Retrieval when the star–companion couple is oriented perpendicular to the longest VLTI baselines. The red curves are the 1σ contrast limits for the best and worst UV plane orientation, shown as thick or thin lines alternatively depending on the background plot.

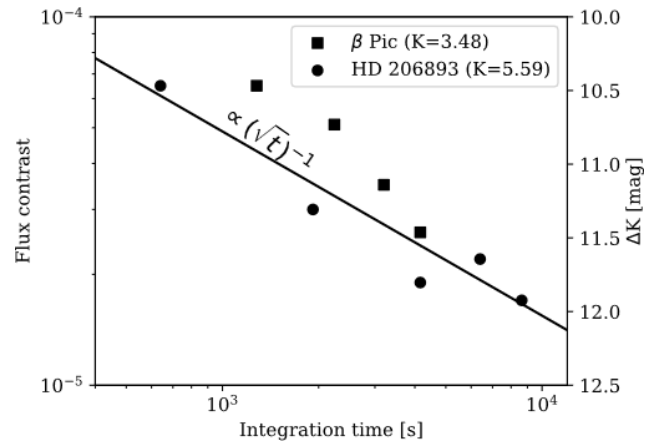**Fig. 10.** Limit contrasts at 1σ with respect to the total exposure time (NEXP × NDIT × DIT). The solid line corresponds to the inverse square root of the integration time, with a proportionality constant of 1.5×10^{-3} in flux contrast.

Table 3. Parameters for the computation of the theoretical contrast curve.

Parameter	Value
DIT	10 s
$NDIT_{tot}$	160
RON	9 photons/DIT
N_{pixels} [a]	11 184
Fluxes	
T_0 [b]	1 %
F_s [c]	7×10^8 photons s^{-1}
V_c [d]	$0.8 \times F_c$

Notes. [a]There are 24 ABCD outputs on the detector, 233 pixels in the spectral direction, and the spectrum is two pixels wide. [b]Total transmission of the VLTI and GRAVITY when the SC fiber is at 0 mas separation. [c]Flux of HD 206893 for a single telescope. Computed from the star magnitude in K-band and the UT collecting surface. [d]We estimate the instrumental visibility to be 0.8.

integration time. Instead, we observe that the detection limit follows a similar $\sqrt{t}^{-1}$ trend for both stars. This indicates that the detection is not limited by photon noise, but by other features that are still averaging over the integration time. The situation is similar in classical imaging where the detection limit evolves with the characteristic lifetime of the speckles in the field. From an operational point of view, we can conclude that extending the integration time up to 90 min is a way to push the contrast limit down to 2×10^{-5} ($\Delta K = 11.7$ mag) at 100 mas.

Overall, GRAVITY seems to be limited by systematic uncertainties that scale with the speckle flux. This explains why the off-pointing technique described in Sect. 2.2.1 has a significant impact on the detection limit, as would any further reduction of the stellar leak.

4.3. Comparison with the theoretical limit

The detection limits can also be determined analytically. Considering the photon noise from the star flux leaking in the fiber at the companion position and the readout noise of the SC camera, we can derive a S/N using

$$S/N =$$
$$\frac{\eta \sum_{b,\lambda} |G(b,\lambda) V_c(b,\lambda)| \, DIT \, NDIT_{tot}}{\sqrt{\sum_{m,\lambda} T(m,\lambda) F_s(m,\lambda) \, DIT \, NDIT_{tot} + RON^2 \, N_{pixels} \, NDIT_{tot}}}, \tag{15}$$

where η is the fraction of companion signal remaining after subtracting the speckles polynomial, $NDIT_{tot}$ is the total number of integrations (NEXP × NDIT), RON is the read-out noise of the SC camera (Teledyne H2RG), and N_{pixels} is the number of pixels used on the detector. The other parameters are described in Eqs. (2) and (4).

From Eq. (15) and parameter values listed in Table 3, we can derive a limiting planet-to-star contrast for a given S/N. The results are shown in Fig. 11. The photon noise from the star largely dominates the statistical noise. The detection limit at $S/N = 1$ allows direct comparison with the 1σ empirical contrast curve. This comparison shows that the theoretical detection limits are a factor 12 lower than the empirical detection limits determined from injection and retrieval. We show in Sect. 4.2
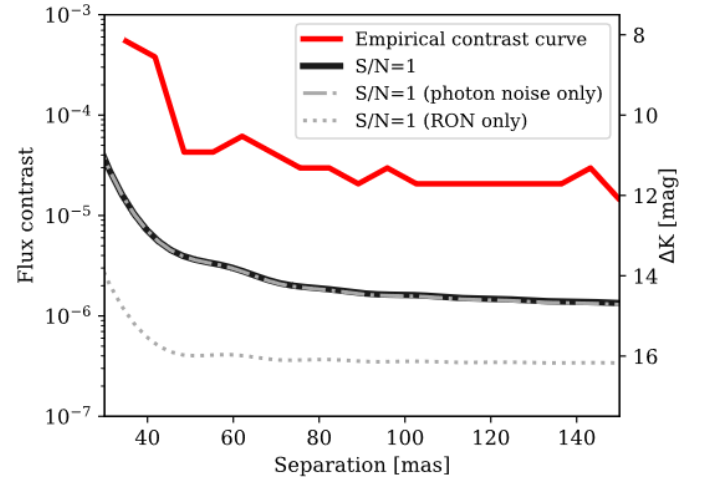
Fig. 11. Theoretical contrast curves for $S/N = 1$ (solid black) compared to the contrast curve derived from the injection and retrieval at a favorable positional angle (red). An indicative contrast curve is given with only the camera readout noise as a noise source (dotted black) and only the photon noise (dashed-dotted black). The theoretical contrast curves are computed for a host star of K-band magnitude 5.6 similar to HD 206893 used in the injection–retrieval data set.

that photon noise is not the limitation in actual observations at 100 mas separation. The findings shown in this section confirm that result.

5. Discussion

5.1. Summary

In this paper, we detail a proposed observing strategy and adjustment of the data reduction pipeline required to enable exoplanet observations at shorter separations with GRAVITY. We validated the proposed strategy and demonstrated the *Gaia*–GRAVITY synergy with the detection and mass determination of the short-separation companion *Gaia*...6464 B. We finally explored the actual capabilities of GRAVITY by deriving realistic contrast curves. The most important results of this work can be summarized as follows:

– The fiber off-pointing strategy brings a contrast improvement of up to a factor of six for dual-field observations of companions below 80 mas separation. The implementation of this technique is straightforward;

– The inner working angle has become narrower since the upgrade of the GRAVITY FT. Below 45 mas, fitting the stellar speckles with a third-order polynomial gives better results than the fourth or sixth-order polynomials previously recommended;

– Our detection of the brown dwarf *Gaia*...6464 B shows how the combination of *Gaia* and GRAVITY leads to a precise measurement of the dynamical masses of the companion ($78.34^{+2.62}_{-2.50}\,M_{Jup}$) and the primary ($0.53^{+0.02}_{-0.02}\,M_\odot$). The detection of the brown dwarf is an archetypal example of a GRAVITY observation at the edge of the inner working angle;

– In dual-field mode, GRAVITY can observe companions at contrasts of 4×10^{-5} ($\Delta K = 11$ mag) down to a separation of 75 mas. Due to the limited sampling of the UV plane on the UT, the detection limits below 100 mas are strongly affected by the relative orientation between the primary/secondary and the longest baselines;
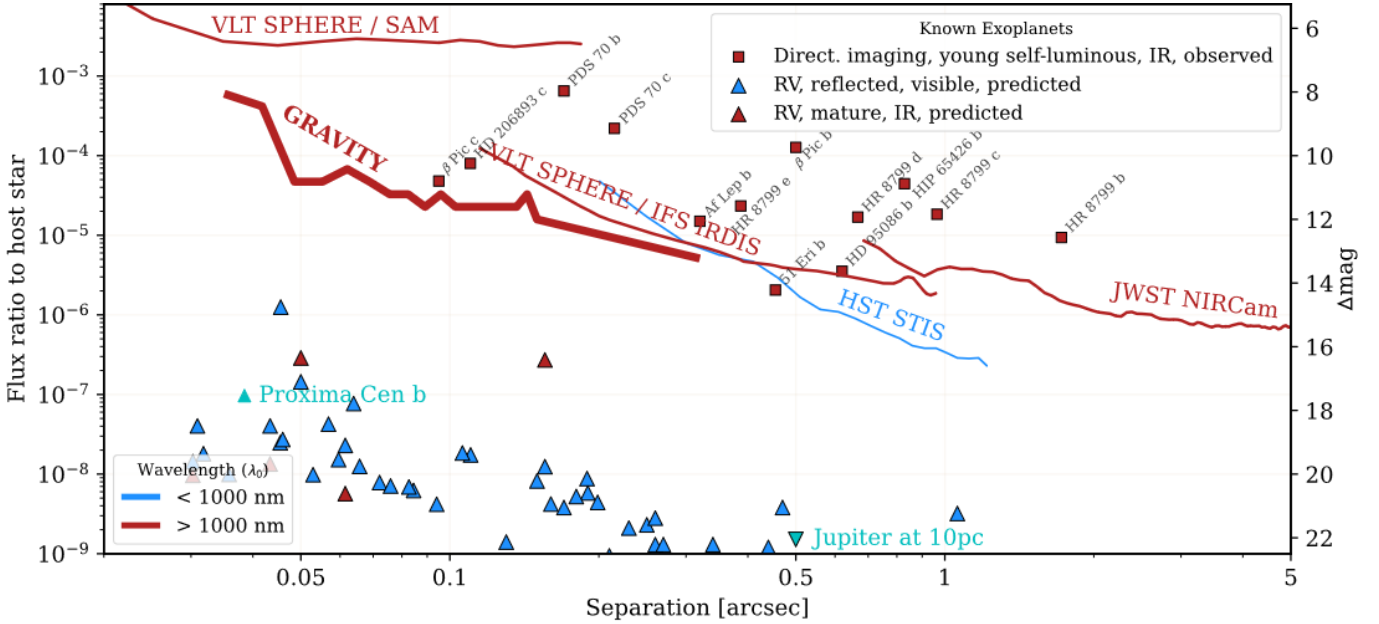
Fig. 12. Detection limits of some representative instruments dedicated to direct observations of exoplanets. GRAVITY detection limit corresponds to the inner part of the on-axis mode of the instrument only. It is limited to 27 min exposure time and companions oriented parallel to the longest baselines of the VLTI. Plot adapted from Dr. Bailey script available at `https://github.com/nasavbailey/DI-flux-ratio-plot`. The HST/STIS curve is from Ren et al. (2017). VLT SPHERE/IFS IRDIS is from Langlois et al. (2021). VLT SPHERE/SAM is from Stolker et al. (2024). VLT JWST/NIRCam is from Carter et al. (2023). (Blue triangles) Estimated reflected flux in the visible for exoplanets observed using the radial velocity technique. The estimation follows a Lambertian model with radii fixed at 1 R_{Jup} and a geometric albedo of 0.5. (Red triangle) Estimated infrared flux for mature exoplanets observed using the radial velocity technique. Computed from equilibrium temperature estimates and planet radii fixed at 1 R_{Jup}. All visible and infrared estimated fluxes are based on Traub & Oppenheimer (2010).

– Observing the same target for about 3h pushes the detection limit down to 2×10^{-5} ($\Delta K = 11.7$ mag) at 100 mas. The limiting factor appears to be speckle structures whose amplitude scales with the coherent flux and that slowly average over time.

These findings are the result of experience gained over 5 yr of exoplanet and brown dwarf observations with GRAVITY. A better understanding of the instrument enabled us to identify promising avenues for improving observations and to consider possible synergies with other instruments.

5.2. Comparison with other direct imaging instruments

Figure 12 compares the contrast curve of GRAVITY estimated in this paper with those of some other exoplanet-imaging instruments. This paper focuses on companion observations with GRAVITY below 300 mas separation. However, it should be noted that the off-axis mode of the instrument allows observations at separations of up to 2 arcsec on the UT. For separations of greater than 200 mas, the detection capabilities of GRAVITY are comparable to single-telescope imagers. Indeed, all exoplanets directly imaged with SPHERE at the VLT have also been detected with GRAVITY. GRAVITY is especially useful because of its 50 µas precision in relative astrometry and its higher spectral resolution. For long-period orbits, the accurate astrometry of GRAVITY can constrain orbital parameters within a few years. Moreover, these accurate astrometric observations will adequately complement further observations at the same level of accuracy as should be achieved by the E-ELT, providing a large time baseline.

Closer than 200 mas, GRAVITY is unique because this region is mostly beyond the reach of current single-telescope instruments. For instance, β Pictoris c and HD 206893 c are easily detected by GRAVITY but have so far remained undetected by SPHERE or GPI. We note that the molecular mapping technique is being increasingly used for exoplanet detection and characterization (Vigan et al. 2024). Molecular mapping has formally no self-subtraction inner working angle (unlike the spectral or angular differential deconvolutions). Instead, the method relies on the signal provided by sharp spectral features in the companion spectra, and is therefore highly photon consuming and requires longer integration times; it is blind to the continuum part of the spectrum, including the absolute flux of the companion. This is complementary to GRAVITY observations at moderate spectral resolution. The question of whether or not the molecular mapping technique can be applied to GRAVITY data themselves remains unanswered.

5.3. Synergy with Gaia

Brown dwarf companion candidates are already available in *Gaia* DR3. The next *Gaia* DR4 will provide the individual epochs of the stellar proper motion and a catalog of possibly thousands of planetary-mass companions suitable for characterization from the ground.

Figure 13 combines the GRAVITY detection limits derived in this paper with the expected *Gaia* sensitivity to substellar companions (Sozzetti 2010). This comparison shows that the GRAVITY sensitivity already overlaps with the *Gaia* sensitivity to companions in the 50 to 100 mas separation range around the nearest stars. Thus, GRAVITY bridges the gap for direct detection of these *Gaia* candidates before the E-ELT instruments (Houllé et al. 2021). We note that Fig. 13 uses the favorable
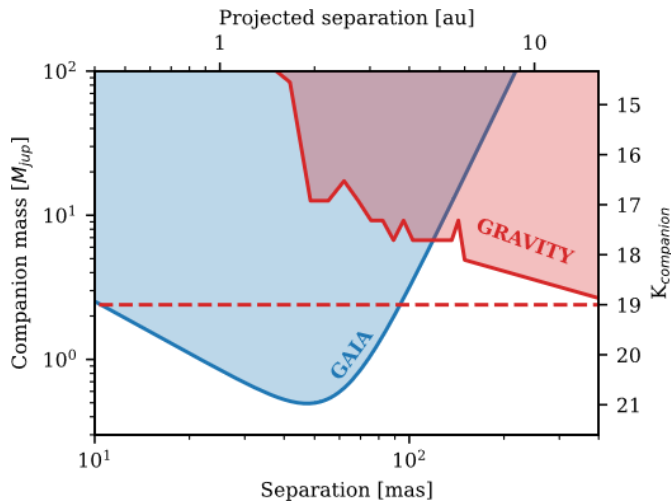
Fig. 13. Comparison of the sensitivity of *Gaia* and GRAVITY for a *K*=6 mag star at 40 pc. The *Gaia* sensitivity curve is adapted from Sozzetti (2010). The scaling of the K-magnitude with the mass is estimated from the observations of *Gaia*...6464 B analyzed in this paper and previous companion observations from the ExoGRAVITY program. The dashed red line shows the current K-magnitude limit in the SC of GRAVITY.

case of a star located at 40 pc to convert the linear and angular separation. For more distant stars, the *Gaia* sensitivity peak shifts toward even shorter angular separation. This highlights the interest of the unique inner working angle of GRAVITY and emphasizes the importance of pushing the instrument to even shorter separations and deeper contrast.

5.4. Perspectives with GRAVITY+

The GRAVITY+ upgrade includes a faint mode that turns off the metrology lasers during the acquisitions to provide better S/N for faint targets (Widmann et al. 2022) and a new extreme AO at the Coudé focus of the four UTs (Eisenhauer 2019). The replacement of the 20 yr-old MACAO will significantly improve the wavefront correction for atmospheric turbulence and enable correction of instrument internal aberrations (not possible with the current AO). The expected performance is a Strehl ratio of about 0.8 on natural guide stars, compared with the ratio of ~0.3 presently provided by MACAO. This fact alone will already contribute to limiting the starlight injection at the planet's position by a factor 3 to 4. However, it is possible to go even further. The higher level of AO performance will allow wavefront control techniques to further reduce the starlight at the fiber position when observing the companion (Pourré et al. 2022). The technique consists in injecting offset modes in the AO to tackle diffraction and static aberrations that couple into the SC fiber. Assuming a telescope close to the diffraction limit, and together with the fiber position offset presented in this paper, this technique could reduce the speckle amplitude by up to two orders of magnitude at separations of from 60 to 140 mas. In real conditions on-sky, Xin et al. (2023) showed that wavefront control on KPIC can result in up to a factor 3 reduction in *K*-band stellar flux injected into a single-mode fiber at $2 \lambda/D$. It indicates that, overall, the developments at VLTI and GRAVITY might push the contrast limits to 3×10^{-6} ($\Delta K = 13.8$ mag) down to 60 mas separation. For the closest stars in our galactic neighborhood, this will enable observations of the young Jupiter-mass planets, possibly down to the snowline at 2 to 5 au from their star.

References

Abuter, R., Dembet, R., Lacour, S., et al. 2016, SPIE Conf. Ser., 9907, 990721
Anugu, N., Amorim, A., Gordo, P., et al. 2018, MNRAS, 476, 459
Arsenault, R., Alonso, J., Bonnet, H., et al. 2003, SPIE Conf. Ser., 4839, 174
Astropy Collaboration (Price-Whelan, A. M., et al.) 2018, AJ, 156, 123
Babusiaux, C., Fabricius, C., Khanna, S., et al. 2023, A&A, 674, A32
Beuzit, J. L., Vigan, A., Mouillet, D., et al. 2019, A&A, 631, A155
Boccaletti, A., Chauvin, G., Wildi, F., et al. 2022, SPIE Conf. Ser., 12184, 121841S
Bonnell, I. A., Clark, P., & Bate, M. R. 2008, MNRAS, 389, 1556
Boss, A. P. 1997, Science, 276, 1836
Bowler, B. P., Blunt, S. C., & Nielsen, E. L. 2020, AJ, 159, 63
Carter, A. L., Hinkley, S., Kammerer, J., et al. 2023, ApJ, 951, L20
Davies, R., Absil, O., Agapito, G., et al. 2023, A&A, 674, A207
Eisenhauer, F. 2019, in The Very Large Telescope in 2030, 30
Foreman-Mackey, D., Hogg, D. W., Lang, D., & Goodman, J. 2013, PASP, 125, 306
Franson, K., Bowler, B. P., Brandt, T. D., et al. 2022, AJ, 163, 50
Gaia Collaboration (Vallenari, A., et al.) 2023, A&A, 674, A1
GRAVITY Collaboration (Abuter, R., et al.) 2017, A&A, 602, A94
GRAVITY Collaboration (Nowak, M., et al.) 2020, A&A, 633, A110
GRAVITY Collaboration (Abuter, R., et al.) 2021, A&A, 647, A59
GRAVITY Collaboration (Abuter, R., et al.) 2022, A&A, 657, A82
GRAVITY+ Collaboration (Abuter, R., et al.) 2022, The Messenger, 189, 17
Halbwachs, J.-L., Pourbaix, D., Arenou, F., et al. 2023, A&A, 674, A9
Harris, C. R., Millman, K. J., van der Walt, S. J., et al. 2020, Nature, 585, 357
Hinkley, S., Carter, A. L., Ray, S., et al. 2022, PASP, 134, 095003
Hinkley, S., Lacour, S., Marleau, G. D., et al. 2023, A&A, 671, A5
Holl, B., Sozzetti, A., Sahlmann, J., et al. 2023, A&A, 674, A10
Houllé, M., Vigan, A., Carlotti, A., et al. 2021, A&A, 652, A67
Hunter, J. D. 2007, Comput. Sci. Eng., 9, 90
Jovanovic, N., Delorme, J. R., Bond, C. Z., et al. 2019, ArXiv e-prints, [arXiv:1909.04541]
Lacour, S., Dembet, R., Abuter, R., et al. 2019, A&A, 624, A99
Lacour, S., Wang, J. J., Rodet, L., et al. 2021, A&A, 654, L2
Langlois, M., Gratton, R., Lagrange, A. M., et al. 2021, A&A, 651, A71
Lapeyrere, V., Kervella, P., Lacour, S., et al. 2014, SPIE Conf. Ser., 9146, 91462D
Leclerc, A., Babusiaux, C., Arenou, F., et al. 2023, A&A, 672, A82
Lozi, J., Ahn, K., Clergeon, C., et al. 2022, SPIE Conf. Ser., 12185, 1218533
Macintosh, B., Graham, J. R., Ingraham, P., et al. 2014, PNAS, 111, 12661
Marois, C., Lafrenière, D., Doyon, R., Macintosh, B., & Nadeau, D. 2006, ApJ, 641, 556
Meshkat, T., Bonnefoy, M., Mamajek, E. E., et al. 2015, MNRAS, 453, 2378
Mizuno, H. 1980, Progr. Theoret. Phys., 64, 544
Nielsen, E. L., De Rosa, R. J., Macintosh, B., et al. 2019, AJ, 158, 13
Nowak, M., Lacour, S., Lagrange, A. M., et al. 2020, A&A, 642, L2
Nowak, M., Lacour, S., Abuter, R., et al. 2024, A&A, in press, https://doi.org/10.1051/0004-6361/202449504

Otten, G. P. P. L., Vigan, A., Muslimov, E., et al. 2021, A&A, 646, A150
Perraut, K., Jocou, L., Berger, J. P., et al. 2018, A&A, 614, A70
Pfuhl, O., Haug, M., Eisenhauer, F., et al. 2012, SPIE Conf. Ser., 8445, 84451U
Por, E. H., Haffert, S. Y., Radhakrishnan, V. M., et al. 2018, Proc. SPIE, 10703, , 1070342
Pourré, N., Le Bouquin, J.-B., Woillez, J., et al. 2022, SPIE Conf. Ser., 12183, 121830V
Racine, R., Walker, G. A. H., Nadeau, D., Doyon, R., & Marois, C. 1999, PASP, 111, 587
Ren, B., Pueyo, L., Perrin, M. D., Debes, J. H., & Choquet, É. 2017, SPIE Conf. Ser., 10400, 1040021
Sozzetti, A. 2010, EAS Pub. Ser., 45, 273
Sparks, W. B., & Ford, H. C. 2002, ApJ, 578, 543
Stolker, T., Kammerer, J., Benisty, M., et al. 2024, A&A, 682, A101
Stone, J. M., Skemer, A. J., Hinz, P. M., et al. 2018, AJ, 156, 286
Traub, W. A., & Oppenheimer, B. R. 2010, in Exoplanets, ed. S. Seager (Tucson, AZ: University of Arizona Press), 111
Vigan, A., Fontanive, C., Meyer, M., et al. 2021, A&A, 651, A72
Vigan, A., El Morsy, M., Lopez, M., et al. 2024, A&A, 682, A16
Wang, J. J., Kulikauskas, M., & Blunt, S. 2021a, Astrophysics Source Code Library, [record ascl:2101.003]
Wang, J. J., Vigan, A., Lacour, S., et al. 2021b, AJ, 161, 148
Widmann, F., Gillessen, S., Ott, T., et al. 2022, SPIE Conf. Ser., 12183, 121830U
Winterhalder, T. O., Lacour, S., Mérand, A., et al. 2024, A&A, submitted [arXiv:2403.13055]
Woillez, J., Abad, J. A., Abuter, R., et al. 2019, A&A, 629, A41
Xin, Y., Xuan, J. W., Mawet, D., et al. 2023, J. Astron. Telescopes Instrum. Syst., 9, 035001

[1] Univ. Grenoble Alpes, CNRS, IPAG, 38000 Grenoble, France
e-mail: nicolas.pourre@univ-grenoble-alpes.fr

[2] European Southern Observatory, Karl-Schwarzschild-Straße 2, 85748 Garching, Germany

[3] LESIA, Observatoire de Paris, PSL, CNRS, Sorbonne Université, Université de Paris, 5 place Janssen, 92195 Meudon, France

[4] Institute of Astronomy, University of Cambridge, Madingley Road, Cambridge CB3 0HA, UK

[5] Universidade de Lisboa – Faculdade de Ciências, Campo Grande, 1749-016 Lisboa, Portugal

[6] CENTRA – Centro de Astrofísica e Gravitação, IST, Universidade de Lisboa, 1049-001 Lisboa, Portugal

[7] Max Planck Institute for Astronomy, Königstuhl 17, 69117 Heidelberg, Germany

[8] Department of Physics & Astronomy, Johns Hopkins University, 3400 N. Charles Street, Baltimore, MD 21218, USA

[9] Space Telescope Science Institute, 3700 San Martin Drive, Baltimore, MD 21218, USA

[10] Center for Interdisciplinary Exploration and Research in Astrophysics (CIERA) and Department of Physics and Astronomy, Northwestern University, Evanston, IL 60208, USA

[11] Max Planck Institute for extraterrestrial Physics, Giessenbachstraße 1, 85748 Garching, Germany

[12] Aix-Marseille Univ, CNRS, CNES, LAM, Marseille, France

[13] Université Côte d'Azur, Observatoire de la Côte d'Azur, CNRS, Laboratoire Lagrange, Bd de l'Observatoire, CS 34229, 06304 Nice cedex 4, France

[14] STAR Institute, Université de Liège, Allée du Six Août 19c, 4000 Liège, Belgium

[15] Leiden Observatory, Leiden University, PO Box 9513, 2300 RA Leiden, The Netherlands

[16] Department of Astrophysical & Planetary Sciences, JILA, Duane Physics Bldg., 2000 Colorado Ave, University of Colorado, Boulder, CO 80309, USA

[17] Institute of Astronomy, KU Leuven, Celestijnenlaan 200D, 3001 Leuven, Belgium

[18] Institute of Physics, University of Cologne, Zülpicher Straße 77, 50937 Cologne, Germany

[19] Max Planck Institute for Radio Astronomy, Auf dem Hügel 69, 53121 Bonn, Germany

[20] Universidade do Porto, Faculdade de Engenharia, Rua Dr. Roberto Frias, 4200-465 Porto, Portugal

[21] School of Physics, University College Dublin, Belfield, Dublin 4, Ireland

[22] School of Physics & Astronomy, University of Southampton, University Road, Southampton SO17 1BJ, UK

[23] Departments of Physics and Astronomy, Le Conte Hall, University of California, Berkeley, CA 94720, USA

[24] European Southern Observatory, Casilla 19001, Santiago 19, Chile

[25] Advanced Concepts Team, European Space Agency, TEC-SF, ESTEC, Keplerlaan 1, 2201 AZ Noordwijk, The Netherlands

[26] University of Exeter, Physics Building, Stocker Road, Exeter EX4 4QL, UK

[27] Fakultät für Physik, Universität Duisburg-Essen, Lotharstraße 1, 47057 Duisburg, Germany

[28] Institüt für Astronomie und Astrophysik, Universität Tübingen, Auf der Morgenstelle 10, 72076 Tübingen, Germany

[29] Center for Space and Habitability, Universität Bern, Gesellschaftsstrasse 6, 3012 Bern, Switzerland

[30] Astronomy Department, University of Michigan, Ann Arbor, MI 48109 USA

[31] Academia Sinica, Institute of Astronomy and Astrophysics, 11F Astronomy-Mathematics Building, NTU/AS campus, No. 1, Section 4, Roosevelt Rd., Taipei 10617, Taiwan

[32] European Space Agency (ESA), ESA Office, Space Telescope Science Institute, 3700 San Martin Drive, Baltimore, MD 21218, USA

[33] Department of Earth & Planetary Sciences, Johns Hopkins University, Baltimore, MD, USA

[34] Max Planck Institute for Astrophysics, Karl-Schwarzschild-Str. 1, 85741 Garching, Germany

[35] Excellence Cluster ORIGINS, Boltzmannstraße 2, 85748 Garching bei München, Germany

[36] DOTA, ONERA, 13661 Salon cedex AIR, France

[37] KRP Mechatec GmbH, Boltzmannstraße 2, 85748 Garching bei München, Germany

[38] Universidad de Valparaíso, Instituto de Física y Astronomía (IFA), Avenida Gran Bretaña 1111, Casilla 5030, Valparaíso, Chile

[39] Núcleo Milenio de Formación Planetaria (NPF), Valparaíso, Chile

[40] Univ. Lyon 1, ENS de Lyon, CNRS, Centre de Recherche Astrophysique de Lyon UMR5574, 69230, Saint-Genis-Laval, France

Appendix A: Complex visibilities for a planet detection on GRAVITY

Figure A.1 shows how we retrieve the companion signal buried in the speckle flux. The ExoGRAVITY reduction script performs a joint fit of the speckles and the planet on the complex visibilities. The correlated and uncorrelated noises can be seen in Fig. A.1b, especially on the U4-U3 and U3-U2 baselines, that provide a weak planet signal.
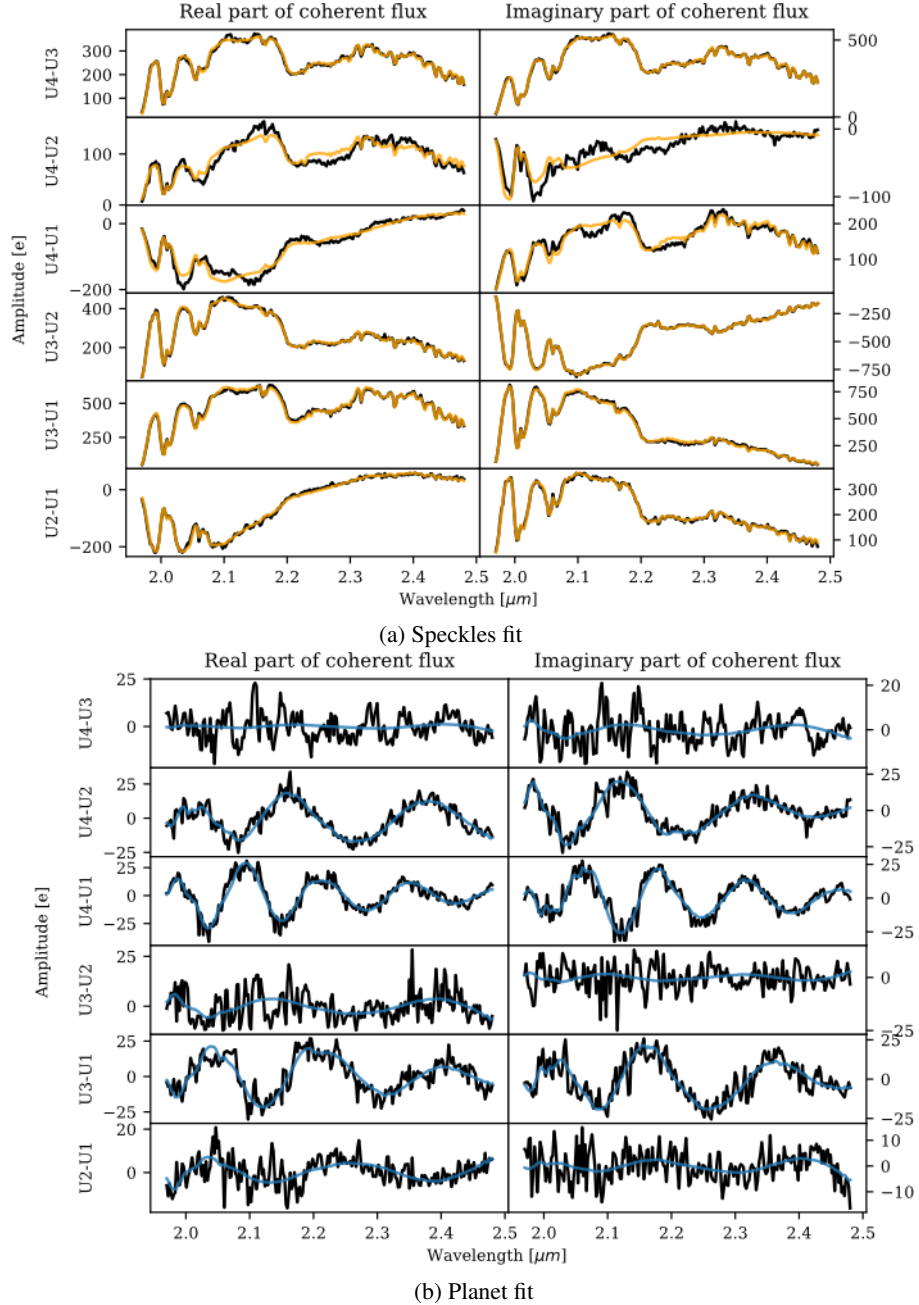

(a) Speckles fit

(b) Planet fit

Fig. A.1: Example of speckle fit (a) and planet fit (b) in GRAVITY complex visibilities for an injected companion at 68 mas separation and 8×10^{-4} contrast. (a) Black: Complex visibilities $V_{\mathrm{oncompanion}}$ as outputted by the general GRAVITY pipeline and phase referenced on the star. Orange: Speckles fit with the polynomial modulation corresponding to the first term in Eq. (9). (b) Black: $V_{\mathrm{oncompanion}}$ with the speckle fit subtracted. Blue: Planet fit, corresponding to the second term in Eq. (9)

Appendix B: ExoGRAVITY observations used for detection limits

For the companion injection and retrieval, we used archival Exo-GRAVITY observations. We chose the observations based on the criteria of the relative separation of the SC fiber from the star, and good atmospheric conditions. Data sets are detailed in Table B.1.

Table B.1: Details of the ExoGRAVITY observations used for the companion injection and retrievals.

Injection separation limits	30 to 45 mas	45 to 70 mas
SC fiber separation [mas]	54	72
Target star	HD 17155	HD 206893[a]
Date	2022-08-19	2021-08-28
K star [mag]	6.5	5.6
Seeing [arcsec]	0.54	0.62
τ_0 [ms]	9-18	2-8
Integration time	$5 \times 32 \times 10$ s	$5 \times 32 \times 10$ s
Injection separation limits	70 to 100 mas	100 to 130 mas
SC fiber separation [mas]	92	111
Target star	β Pictoris	HD 206893
Date	2021-01-06	2021-10-17
K star [mag]	3.5	5.6
Seeing [arcsec]	0.45	0.50
τ_0 [ms]	8-12	2-4
Integration time	$5 \times 32 \times 10$ s	$5 \times 32 \times 10$ s
Injection separation limits	130 to 150 mas	320 mas
SC fiber separation [mas]	136	320
Target star	β Pictoris	AF Leporis
Date	2020-02-10	2023-12-23
K star [mag]	3.5	4.9
Seeing [arcsec]	0.81	0.52
τ_0 [ms]	6-15	5-10
Integration time	$5 \times 32 \times 10$ s	$5 \times 12 \times 30$ s

Notes. [a]The observations of HD 206893 on 2021-08-28 were performed in a search for the HD 206893 c planet and no planet was detected in this data set.